Micro-Precision Interferometer:
evaluation of new disturbance isolation solutions

John F. O'Brien, Renaud Goullioud, and Gregory W. Neat

Jet Propulsion Laboratory, California Institute of Technology, CA 91009, Pasadena, USA

ABSTRACT

This paper describes a benchmark to assess performance of six-axis vibration isolation systems. The targeted application, spaceborne interferometers, require isolation of the reaction wheel disturbances in order to stabilize the precision optical elements to the required levels. The problem is to isolate this vibrating payload from the quiet structure (spacecraft). The unique feature of this procedure is that isolator performance is measured in terms of the stabilities of the interferometer optical elements. Central to the procedure is the Micro-Precision Interferometer (MPI) testbed which is a hardware model of a future spaceborne optical interferometer. The isolation system under evaluation is mounted on the testbed and disturbance transfer functions are then measured from the isolator payload to the optical sensor output that must be stabilized. Off-line, the procedure combines these measured testbed tranfer functions with an empirical model of the reaction wheel disturbance, in order predict isolator performance over the entire range of wheel speeds. The paper applies the procedure to four different disturbance interface conditions: hard mounted, passive hexapod isolator, active hexapod isolator and a passive elastomeric isolator. The paper contains all the necessary information to allow industry, academia or other organizations to evaluate custom designs in this testbed facility.

Keywords: Interferometry, Micro-Precision Interferometer, Vibration Isolation, Hexapod, Vibration Attenuation

1. INTRODUCTION

Spaceborne optical interferometers use an array of two or more smaller telescopes, as opposed to a single large telescope, to collect light from a single target star. The light from these telescopes, or sub-apertures, is combined to create an interference fringe pattern. This pattern (optical path difference), which results when the distance from the observed star through each arm of the interferometer to the detector are equal, must be stabilized to the 10 nanometer level for succes,sful instrument operation .[1]

The Stellar Interferometer Mission (SIM) is a first-generation spaceborne interferometer concept with astrometric and imaging goals.[2] Unlike ground-based interferometers bolted to bedrock,[3,4] instrument optics of SIM are distributed across a 10 m, light-weight structure. The primary mechanical disturbance sources exciting the structure are expected to be the spinning reaction wheels used as actuators for the attitude control system. Simulation results suggest that in the unattenuated spacecraft environment, the optical path variation is a factor of one hundred above the 10 nm requirement.[5] This discrepancy inspired the layered vibration attenuation control strategy which involves the blending of vibration isolation, structural quieting, and active optical control.[6] This paper discusses vibration isolation. The isolator must isolate the vibrating reaction wheel payload from the quiet structure which supports the optical elements. High frequency disturbances from the reaction wheels must be attenuated while the isolator must remain rigid at low frequency to enable reaction wheel control torques.

This paper describes a performance evaluation procedure that enables the comparison of different vibration isolation solutions under conditions and with metrics that are representative of those expected on-orbit for spaceborne interferometers. Traditionally, performance assessment of vibration isolation systems has been done by measuring transmisibility from the noisy side to the quiet side on a test bench .[7] When the base or the payload experience flexibility, this approach becomes extremely complex to interpret. In addition, although this strategy provides a quantitative technique for assessing isolator performance on its own, the mechanical boundary conditions are not representative of the on-orbit boundary conditions and it is difficult to extrapolate from the transmissibility results to actual instrument performance, especially in six axes.

Central to this performance evaluation procedure is the Micro-Precision Interferometer (MPI) testbed[8,9] Figure 1 shows a bird's eye view of the MPI testbed. Located at the Jet Propulsion Laboratory, the testbed contains all the subsystems necessary to assess the effectiveness of the vibration attenuation technologies. effectiveness. These subsystems are: a 7 m x 7 m x 6.5 m softly suspended truss structure with mounting plates for subsystem hardware; a six-axis vibration isolation system which can support a reaction wheel assembly to provide a flight-like input disturbance source; a complete Michelson interferometer; internal and external metrology systems; and a star simulator that provides stellar input to the interferometer collecting apertures.
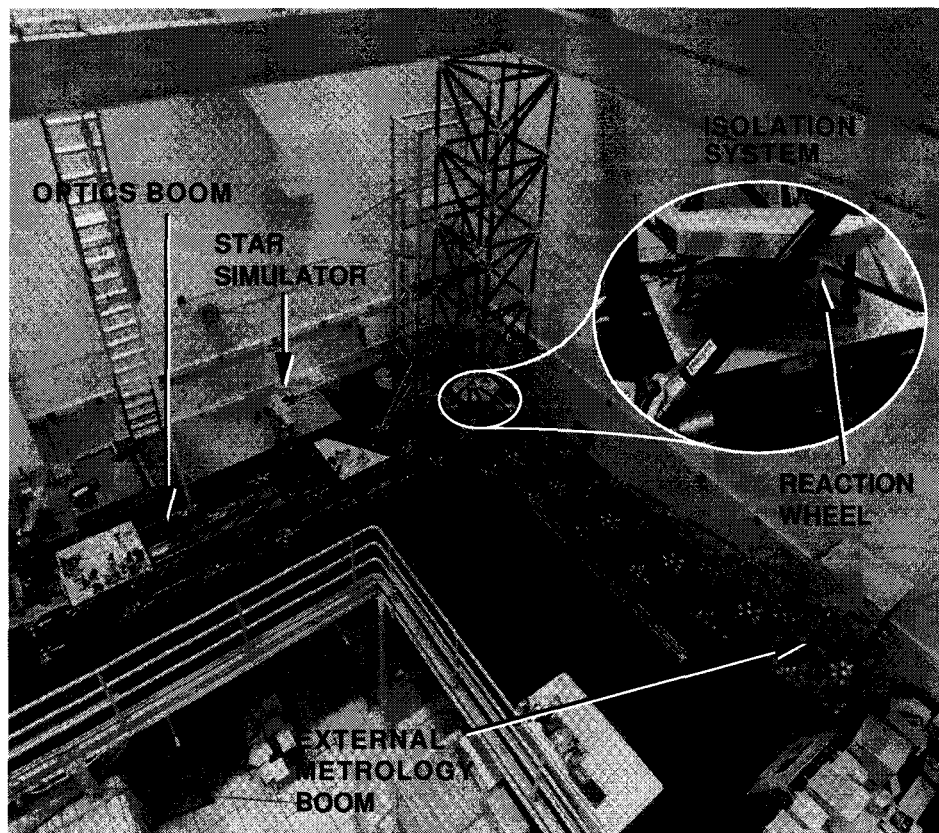
Figure 1. Bird's eye view of the MPI testbed with inset showing a close-up of the six-axis isolation system.

The procedure involves interfacing the isolator under evaluation to the testbed and measuring the requisite disturbance transfer functions in six degrees of freedom. These transfer functions accurately depict (in a linear sense) the effectiveness of the vibration isolation system at achieving nanometer stabilization of the optical elements. Modeled reaction wheel disturbance profiles are then played through this family of measurements to predict the on-orbit performance in terms of the desired metric; nanometers of optical path difference as a function of wheel speed. Applying different norms to these performance functions, the performance metric is simplified to a single number. Using the procedure, the paper compares four disturbance source interface conditions. These include hard mounted (no isolation), passive hexapod isolator, active hexapod isolator, and passive elastomeric isolator. The paper describes the procedure and presents a description of each isolator configuration and the corresponding results from the evaluation procedure. This initial study along with the description of the procedure is intended to encourage industry, academia, or other institutions to interface their custom isolation systems with this testbed facility.

2. ISOLATOR PERFORMANCE EVALUATION

2.1. Procedure Overview

The performance evaluation procedure combines disturbance transfer function measurements from the testbed with an analytical disturbance model, in order to assess isolator performance over the entire range of disturbance conditions

2

expected on-orbit during instrument observations. This hybrid experimental/analytical procedure predicts on-orbit isolator behavior in an accurate, efficient manner. Measuring performance solely in hardware would require measuring the optical metric while stepping through all combinations of wheel speeds for the four reaction wheel assemblies. The time required to perform this measurement is prohibitive. The test would also require having at least one reaction wheel and a suspension system to stabilize the testbed attitude in the presence of the spinning wheel. In addition, the time domain optical sensor data would be corrupted with ambient disturbances not traceable to space such as rigid body motion of the suspended structure, pseudo star motion, atmospheric effects on the laser beams, and acoustic disturbances from the ambient lab environment. Conversely, performing this assessment solely in analysis would require an accurate analytical representation (over all frequencies) of the structure, control system sensors and actuators and the disturbance sources. Attaining the necessary model fidelity is a challenge; especially at higher frequencies ($100Hz$). In addition, it is difficult to accurately represent the actuators and sensors, particularly with respect to practical implementation constraints such as noise floors and dynamic ranges.

Figure 2 shows how the task of accurately representing the on-orbit problem has been distributed between the hardware and analysis tools. The five steps which make up this procedure are: (1) the analytical reaction wheel disturbance model, (2) interfacing the isolator to the testbed, (3) measuring disturbance transfer functions, (4) the performance prediction algorithm, and (5) the calculation of output optical performance metrics.

2.2. Reaction Wheel Disturbance Model

Based on test data obtained from the HST flight units,[10] the disturbance forces and torques are modeled as discrete harmonics of the reaction wheel speed, f_{rwa}, with amplitudes proportional to the wheel speed squared:

$$m(t) = \sum_{i=1}^{n} C_i f_{rwa}^2 \sin\left(2\pi h_i f_{rwa} t + \phi_i\right) \qquad (1)$$

where $m(t)$ is the disturbance torque or force, C_i is an amplitude coefficient, h_i is the harmonic number, and ϕ_i is a random phase (uniform over $[0, 2\pi]$) used to account for phase uncertainty. According to this model, h_i and C_i uniquely determine the amplitude and frequency of each harmonic component for a given wheel speed. Reference[11] gives the values for the different harmonics.

The disturbances modeled are one axial force (along the wheel spin axis), two radial forces (normal to the spin axis), and two radial torques (causing wheel wobble). These disturbances result from wheel imbalances and bearing imperfections.[10] Disturbance torque about the axis of rotation (torque ripple and motor cogging) was found to be insignificant.

The procedure requires reaction wheel disturbance power spectral densities as input to the measured transfer functions. Given that the reaction wheel disturbances are sinusoidal wheel harmonics (Eq. 1), and assuming that the random phases (ϕ_i) are independent, identically-distributed,[12] the power spectral densities consist of Dirac delta functions[13] at the harmonic frequencies:

$$\Phi_m(\omega) = \sum_{i=1}^{n} \frac{\pi C_i^2 f_{rwa}^4}{4} \left[\delta\left(\omega - 2\pi h_i f_{rwa}\right) + \delta\left(\omega + 2\pi h_i f_{rwa}\right)\right] \qquad (2)$$

where $\Phi_m(\omega)$ is the power spectral density of $m(t)$, and $\delta(t)$ is the Dirac delta function. As an example, Figure 3 shows the power spectral density of axial force at a wheel speed of 1500 rpm. In Figure 3 the Dirac delta function peaks are represented as arrows.

2.3. Isolator Interface

The isolation platform is designed to accommodate any six-axis isolator. The only limitation is the device must be able to fit in approximately a one meter cubic volume. Table 1 lists the physical description of the hardware in the setup. The isolator system under test is located between two plates: the base plate, rigidly mounted to the structure and the payload plate which suports the disturbance source.

The base plate is a square plate rigidly mounted to four MPI truss nodes, at each corner of the plate whereas the payload plate is a free hexagonal plate. The location of these two plates is shown in the inset of Figure 1. Both plates are aluminum face sheets plate with 1/4"-20 threaded holes on both faces at a 1 inch spacing to allow mounting of any disturbance or isolation systems on either side of the plates.
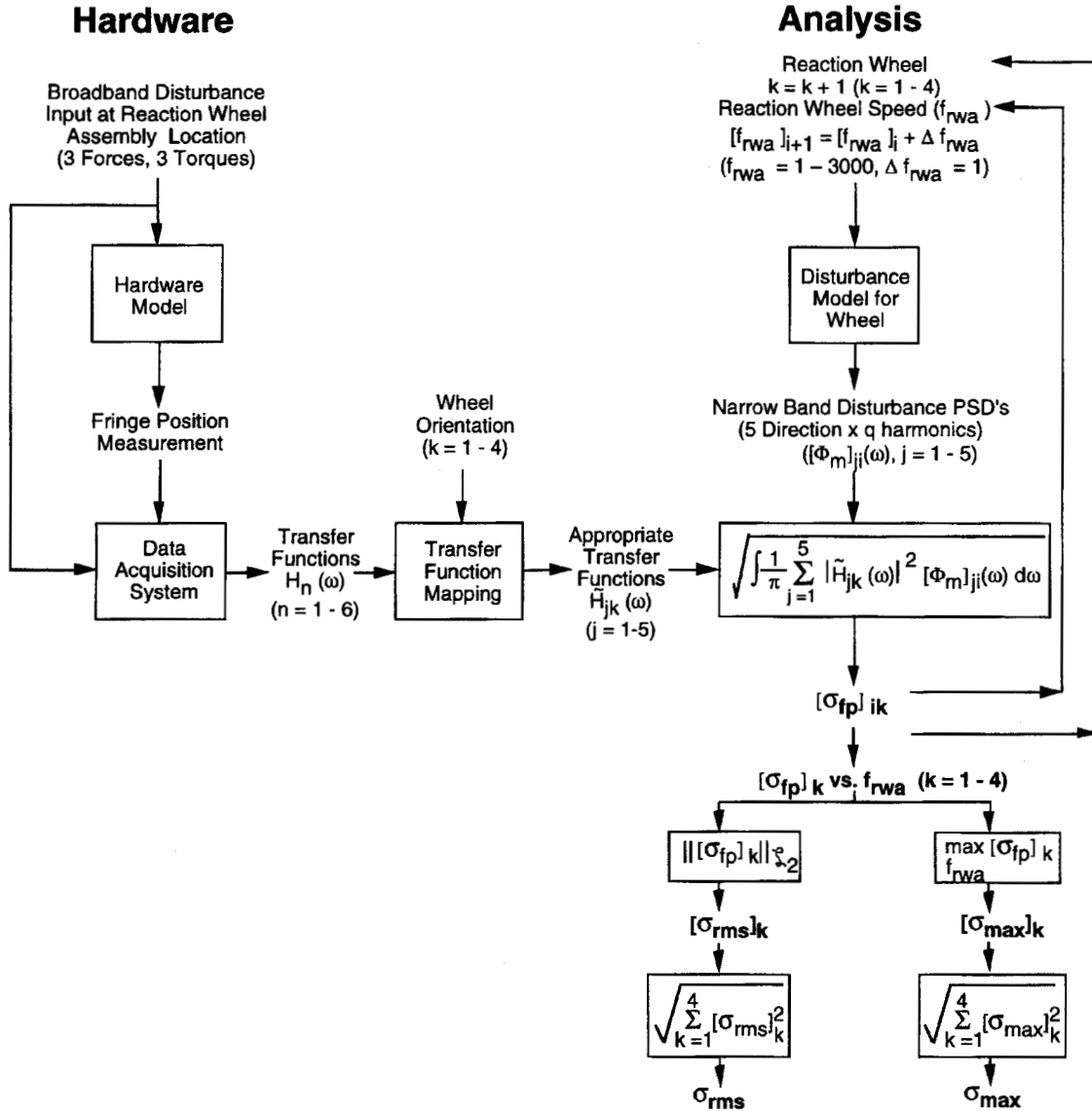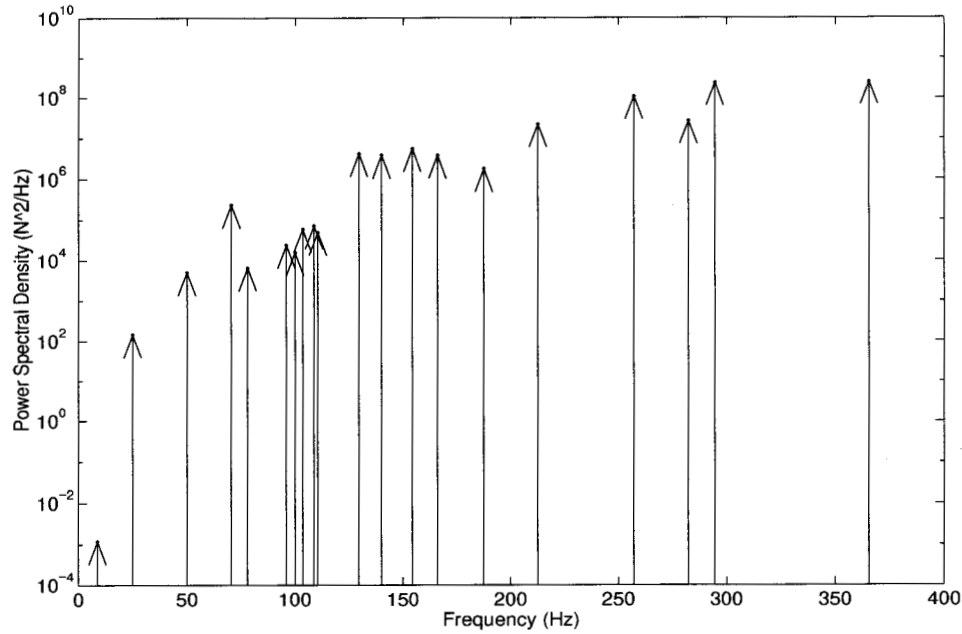
Hardware

Analysis

Broadband Disturbance
Input at Reaction Wheel
Assembly Location
(3 Forces, 3 Torques)

Reaction Wheel
$k = k + 1$ $(k = 1 - 4)$
Reaction Wheel Speed (f_{rwa})
$[f_{rwa}]_{i+1} = [f_{rwa}]_i + \Delta f_{rwa}$
$(f_{rwa} = 1 - 3000, \Delta f_{rwa} = 1)$

Hardware
Model

Disturbance
Model for
Wheel

Fringe Position
Measurement

Wheel
Orientation
$(k = 1 - 4)$

Narrow Band Disturbance PSD's
(5 Direction x q harmonics)
$([\Phi_m]_{ji}(\omega), j = 1 - 5)$

Data
Acquisition
System

Transfer
Functions
$H_n (\omega)$
$(n = 1 - 6)$

Transfer
Function
Mapping

Appropriate
Transfer
Functions
$\tilde{H}_{jk} (\omega)$
$(j = 1\text{-}5)$

$$\sqrt{\int \frac{1}{\pi} \sum_{j=1}^{5} |\tilde{H}_{jk} (\omega)|^2 [\Phi_m]_{ji}(\omega)\, d\omega}$$

$[\sigma_{fp}]_{ik}$

$[\sigma_{fp}]_k$ vs. f_{rwa} $(k = 1 - 4)$

$\| [\sigma_{fp}]_k \|_{\ell_2}$

$\max_{f_{rwa}} [\sigma_{fp}]_k$

$[\sigma_{rms}]_k$

$[\sigma_{max}]_k$

$$\sqrt{\sum_{k=1}^{4} [\sigma_{rms}]_k^2}$$

$$\sqrt{\sum_{k=1}^{4} [\sigma_{max}]_k^2}$$

σ_{rms}

σ_{max}

Figure 2. Isolator performance evaluation procedure.

2.4. Disturbance Transfer Functions

The disturbance source consists of a pair of shakers mounted to a custom six-axis force measuring device (dynamometer). The dynamometer is mounted on the payload plate and measures the forces and torques transmitted to the payload plate. Figure 4 shows the dynamometer on the payload plate with the two shakers.

The dynamometer is a six degrees of freedom disturbance sensor. These six outputs are the three forces (X, Y and Z directions) and the three torques (along the X, Y and Z axis). The mechanical parts consist of the bottom base, 6 load cells, 12 flexures and the top plate. The dynamometer top is a 305 mm circular plate with 1/4"-20 threaded holes at a 1 inch spacing to allow mounting of any kind of disturbance source.

The top plate is mounted to the base of the dynamometer only through the six load cells, three in the vertical direction and three in the horizontal one. The load cells are arranged in a triangular configuration. Two flexures are mounted on each side of the load cell to reduce the coupling between the various load cells. These flexures have to be soft enough the reduce the coupling but hard enough so that the dynamometer modes are located above the frequency range of interest ($750 Hz$).

4

Figure 3. HST reaction wheel axial force disturbance PSD for a wheel spinning at 1500 rpm.

Hardware	Qty	Material	Size	Weight
Base plate	1	Al face sheets Al honeycomb core	square: 795 mm per side 64 mm thick	21.0 kg
Payload plate	1	Al face sheets Al honeycomb core	hegagon: 790 mm apex to apex 60 mm thick	13.3 kg
Dynamometer	1	Al	cylinder: 305 mm diameter 75 mm high	6.2 kg
Shakers	2	Ling Dynamic System max force : 26 N	cylinder: 76 mm diameter 95 mm long	3.2 kg
Proof masses	2	Brass	cylinder: 45 mm diameter 38 mm long	0.5 kg

Table 1. Hardware components description.

Signal conditioning parts consist of the load cell signal amplifier and the arithmetic converter. The Z force (vertical direction), X and Y torques can be determined from the three vertical load cells, whereas, the Z torque and the X and Y forces are determined from the three horizontal load cells. A analog board converts the six signals from the six load cells into six output (X, Y, Z forces and X, Y, Z torques).

An HP signal analyzer is used to measure disturbance transfer functions. The HP unit generates a broadband drive signal. This signal is sent to the two shakers through two power voltage amplifiers. To generate torques, polarity is inverted before one of the shakers. The band-width is divided into 3 ranges (2 - 14.5 Hz, 10 - 110 Hz and 100 - 900 Hz) with a driver voltage increasing with the frequency.

The dynamometer signal conditionner produces a voltage proportionnal to the disturbance. This voltage is sent to the HP analyzer as the input for the transfer function. A custom counter board reads the laser metrology at 8 kHz and a 16 bit digital-to-analog output board generates a voltage proportional to the counter value (i.e. the optical path difference). This signal is sent to the HP analyzer as the output for the transfer function.
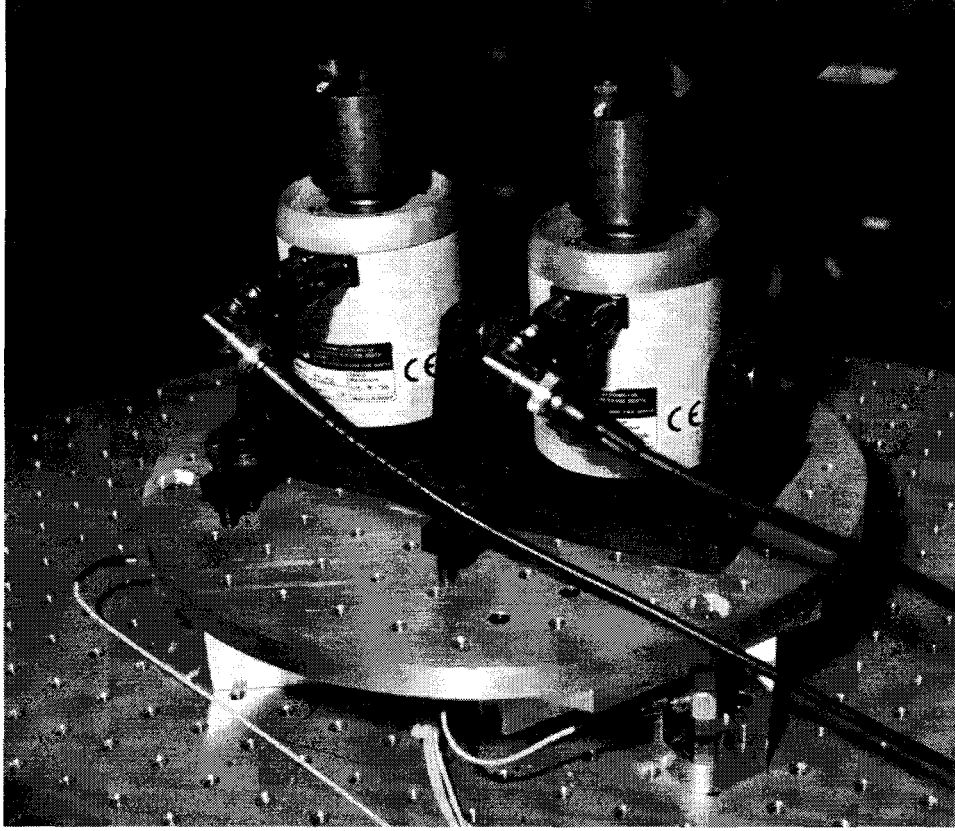
Figure 4. JPL dynamometer with two linear shakers on the top plate producing a Y force.

2.5. Performance Prediction Algorithm

In the analysis environment disturbances of four wheels were modeled, as SIM is expected to carry four RWA's for redundancy. These wheels were assumed to be in a pyramidal configuration, i.e., the axis of each wheel is normal to a side of a square pyramid. The angle of the pyramid was assumed to be 63°, since this yielded equal torque capacity in all three spacecraft axes. Associated with each wheel orientation is a set of RWA local coordinates and a transformation from local to global coordinates. Applying this transformation to the disturbance transfer functions yielded transfer functions from each RWA local disturbance direction to the stellar fringe position for each RWA, as shown in Figure 2. That is, from the six global transfer functions $H_n(\omega)$, twenty local transfer functions, $\tilde{H}_{jk}(\omega)$, were created (five disturbance directions per wheel times four wheels). These twenty transfer functions were then input to the disturbance model algorithm in order to determine fringe position as a function of wheel speed.

The algorithm contains two nested loops with the outer loop indexing each wheel orientation (k=1-4) while the inner loop steps through all possible wheel speeds ($[f_{rwa}]_i = 1$-3000 rpm). The kernel of the algorithm is the calculation of a fringe position standard deviation, $[\sigma_{fp}]_{ik}$, for a single wheel speed (I-index) and orientation (k-index). For each wheel orientation, this calculation begins with five RWA disturbance PSD's generated from the wheel speed, f_{rwa} (an example RWA disturbance PSD is shown in Figure 3. These PSD's, $[\Phi_m]_{ji}(\omega)$, are multiplied by the modulus squared of their corresponding local disturbance transfer functions, $\tilde{H}_{jk}(\omega)$, and summed to yield the fringe position PSD, $[\Phi_{fp}]_{ik}(\omega)$:

$$[\Phi_{fp}]_{ik}(\omega) = \sum_{j=1}^{5} \left| \tilde{H}_{jk}(\omega) \right|^2 [\Phi_m]_{ji}(\omega) \tag{3}$$

An example fringe position PSD is shown in Figure 5, which contains two curves: 1) the discrete-frequency output power spectral density of fringe position as a result of a single wheel spinning at 2596 rpm; 2) the cumulative area

6

under the power spectral density curve. The cumulative area, $\left[\sigma_{fp}^2\right]_{ik}(\omega)$, is calculated by integrating the PSD, $[\Phi_{fp}]_{ik}(\omega)$, over $[0, \omega]$:

$$\left[\sigma_{fp}^2\right]_{ik}(\omega) = \int_0^\omega \frac{1}{\pi}[\Phi_{fp}]_{ik}(\tilde{\omega}) \, d(\tilde{\omega} \tag{4}$$
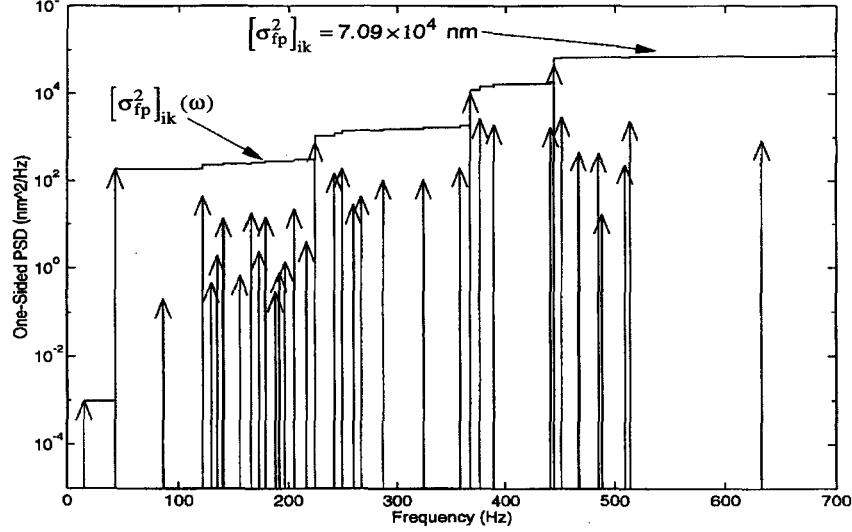
Figure 5. Fringe position power spectral density and cumulative area under the PSD curve for a wheel speed of 2596 rpm.

When the integration limit approaches infinity, the cumulative PSD equals the variance, $\left[\sigma_{fp}^2\right]_{ik}$. The square root of this variance is the fringe position standard deviation, $[\sigma_{fp}]_{ik}$, for a given wheel speed and orientation. This value ($[\sigma_{fp}]_{ik}$) represents a single point in the plot of fringe position variation as a function of wheel speed (RPM). This procedure produces four plots of σ_{fp} vs. f_{rwa}, one for each of the four wheel orientations. For a given plot, each point represents the standard deviation of a discrete-frequency power spectral density. It is not meaningful to combine these four plots into a single plot of σ_{fp} vs. a single wheel speed, since the four wheel speeds are generally not equal.

2.6. Output Metrics

The methodology uses two metrics of overall interferometer performance: one which represents nominal operating conditions and one which represents worts case operating conditions. For each wheel, the worst-case metric, $[\sigma_{\max}]_k$, is the maximum $[\sigma_{fp}]_k(f_{rwa})$ over the range of wheel speeds. The nominal metric, $[\sigma_{rms}]_k$, is the root-mean-square of $[\sigma_{fp}]_k(f_{rwa})$ over the wheel speed (i.e., the square root of the mean variance). Both $[\sigma_{rms}]_k$ and $[\sigma_{\max}]_k$ for each of the four wheel orientations are root-sum-squared to produce a single number as shown in Figure 2.

It is important to note that the mean variance metric, $[\sigma_{rms}]_k$, is actually an L_2 norm:

$$\left[\sigma_{rms}^2\right]_k = \parallel \sigma_{fp} \parallel_{\ell_2}^2 = \frac{1}{f_{\max}} \int_0^{f_{max}} \left[\sigma_{fp}^2\right]_k (F_{rwa}) df_{rwa} \tag{5}$$

where $\parallel \sigma_{fp} \parallel_{\ell_2}$ is the L_2-norm and $f_{\max}$ is the maximum wheel speed. This metric was first applied to the Focus Mission Interferometer in reference.[5] It can be shown that $\parallel \sigma_{fp} \parallel_{\ell_2}$ is equivalent to the standard deviation of fringe position when the wheel speed is a uniform random variable over the interval $[0, f_{\max}]$[14]. Assuming that the wheel speeds are stochastically independent, σ_{rms} can be interpreted as the result of a covariance analysis where the four wheel speeds are assumed to be uniform over $[0, f_{\max}]$. This justifies the interpretation of the mean variance metric as representing nominal operating conditions.

7

# 3. PERFORMANCE COMPARISON OF SPECIFIC ISOLATION SYSTEM DESIGNS

3.1. Isolator Descriptions

Figure 6 shows the two setups that were used to evaluate the four different disturbance interface configurations. The lefthandside in Figure 6 was used to evaluate the hard mounted and elastomeric designs. In each case 1 cm cubes of the respective material were placed at the perifery of the payload plate, spaced 120 degrees apart. For the elastomeric case, these cubes were made of vacuum compatible rubber and held in place with the gravity load of the payload plate. For the hard mounted condition the cubes were made of aluminum and preloaded with a clamp at each of the interface points.
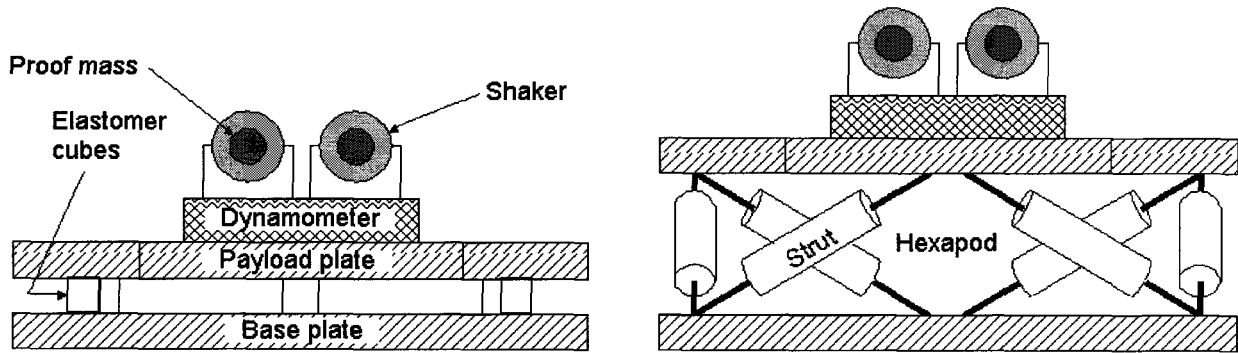
Figure 6. Test configurations used in this study; hard mount and elastomeric (left) hexapod active and passive (right).

The performance prediction algorithm was applied to prototype hexapod design intended for space-based interferometers. Reference[7] provides details on the hexapod design. It consists of six identical struts arranged in a mutually orthogonal configuration. Each strut contains a voice coil with a passive undamped flexure mechanically in parallel. The compensator was implemented digitally and used a voltage driver for the voice coil and a force sensor for the feedback signal. Figure 7 shows the loop gain for a single strut. Each strut utilized the same compensator and was designed as a single-input-single-output system. Performance was assessed for two hexapod configurations: (1) passive and (2) active.
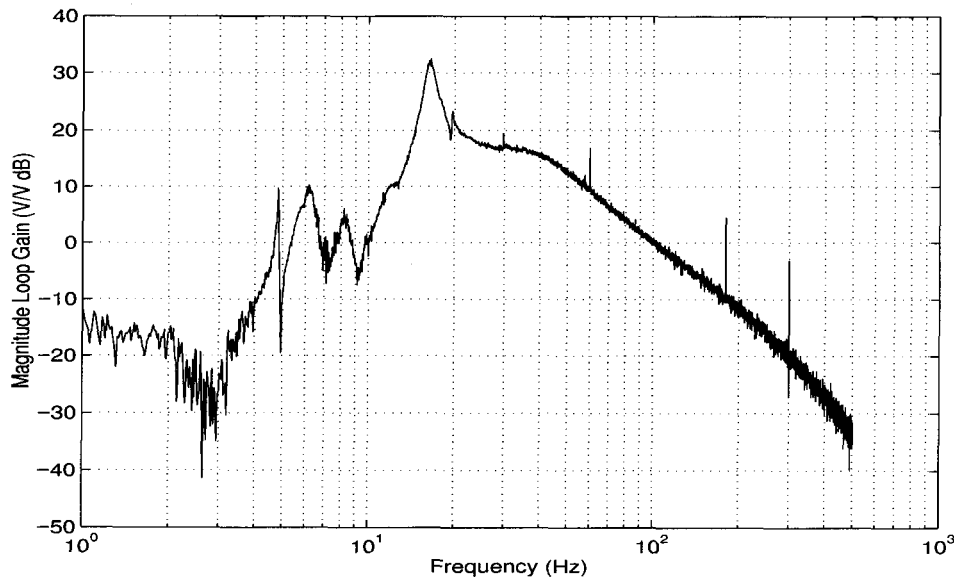
Figure 7. Loop gain for a single strut in the active hexapod.

3.2. Performance Results

Each of the four configurations were evaluated with the same measurement configuration; both in terms of the optical layout and the disturbance input configuration. Figure 8 shows measured disturbance transfer functions for each isolator configuration. The hard mounted condition is plotted on each data set as a reference to compare the degree of isolation over the different frequency ranges.

Figure 9 shows the predicted optical path difference versus wheel speed for the four different conditions. Again, the hard mounted plot is included on each plot for comparison. Finally, Table 2 shows the output metrics for all the different cases tested.

RWA #	Hard-Mount		Elastomeric		Passive Hex		Active Hex	
(k-index)	σ_{rms}	σ_{max}	σ_{rms}	σ_{max}	σ_{rms}	σ_{max}	σ_{rms}	σ_{max}
1	4497	22966	245	1819	537	3377	258	827
2	4201	14739	256	1866	515	3375	257	822
3	3904	21205	243	1826	394	1638	225	1532
4	4594	21517	249	1860	409	1677	237	1535
All	8615	40026	497	3686	936	5250	490	2392

Table 2. Summary of isolator performance results (given in nm).

3.3. Conclusion/Future Work

This paper presents a performance prediction procedure to evaluate six-axis isolation systems. The key feature of the approach is that the performance metric is the actual optical instrument sensor that must be stabilized. This setup is a benchmark to evaluate different isolator designs in the same dynamic environment. The procedure was applied to four different disturbance interface conditions. This paper contains the information necessary to interface other isolator designs from industry, academia or other institutions. Future improvements to the procedure include incorporating all six directions of information from the dynamometer, displaying the output data in three dimensions (rpm vs fringe variation vs frequency) and improving the shaker design. Future isolator activities include improving the compensator design on the present system and evaluating a number of other systems from other institutions.

REFERENCES

1. M. M. Colavita, M. Shao, and M. D. Rayman, "OSI: Orbiting stellar interferometer for astrometry and imaging," in *Special Section on the Williamsburg Space Optics Conference*, 1991.
2. M. Shao and D. M. Wolff, "Orbiting stellar interferometer," in Reasenberg,[14] pp. 228–239.
3. M. Shao, M. M. Colavita, B. E. Hines, D. H. Staelin, D. J. Hutter, K. J. Johnston, D. Mozurkewich, R. S. Simon, J. L. Hersey, J. A. Hughes, and G. H. Kaplan, "Mark III stellar interferometer," *Journal of Astronomy and Astrophysics* **193**, pp. 357–371, 1988.
4. M. M. Colavita, M. Shao, B. E. Hines, J. K. Wallace, Y. Gursel, C. A. Beichman, X. P. Pan, T. Nakajima, and S. R. Kulkarni, "Palomar interferometer testbed," in *Amplitude and Intensity Spatial Interferometry II*, J. B. Breckinridge, ed., vol. 2200 of *Proc. SPIE*, pp. 89–97, (Kona, HI), Mar. 1994.
5. R. A. Laskin and A. M. San Martin, "Control/structure system design of a spaceborne optical interferometer," in *Proc. AAS/AIAA Astrodynamics Specialist Conference*, (Stowe, VT), Aug. 1989.

6. J. T. Spanos, Z. Rahman, C.-C. Chu, and J. F. O'Brien, "Control structure interaction in long baseline space interferometers," in *Proc. 12th IFAC Symposium on Automatic Control in Aerospace*, (Ottobrunn, Germany), Sept. 1992.

7. J. T. Spanos, Z. Rahman, and G. H. Blackwood, "A soft 6-axis active vibration isolator," in *Proc. American Control Conference*, (Seattle, WA), June 1995.

8. G. W. Neat, J. F. O'Brien, N. M. Nerheim, R. J. Calvet, H. Singh, and S. Shaklan, "Micro-precision interferometer testbed: First stabilized stellar fringes," in Reasenberg,[14] pp. 104–115.

9. G. W. Neat, A. Abramovici, J. W. Melody, R. J. Calvet, N. M. Nerheim, and J. F. O'Brien, "Control technology readiness for spaceborne optical interferometer missions," in *Proc. Space Microdynamics and Accurate Control Symposium*, (Toulouse, France), May 1997.

10. M. D. Hasha, "Reaction wheel mechanical noise variations," Engineering Memorandum SSS 218, LMSC, June 1986.

11. J. W. Melody, "Discrete-frequency and broadband reaction wheel disturbance models," Interoffice Memorandum 3411–95–200csi, JPL, June 1995.

12. A. Papoulis, *Probability, Random Variables, and Stochastic Processes*, McGraw-Hill, New York, 3rd ed., 1991.

13. C. H. Edwards and D. E. Penny, *Elementary Differential Equations*, Prentice-Hall, Inc., Englewood Cliffs, NJ, 1985.

14. R. D. Reasenberg, ed., vol. 2447 of *Proc. SPIE*, (Orlando, FL), Apr. 1995.
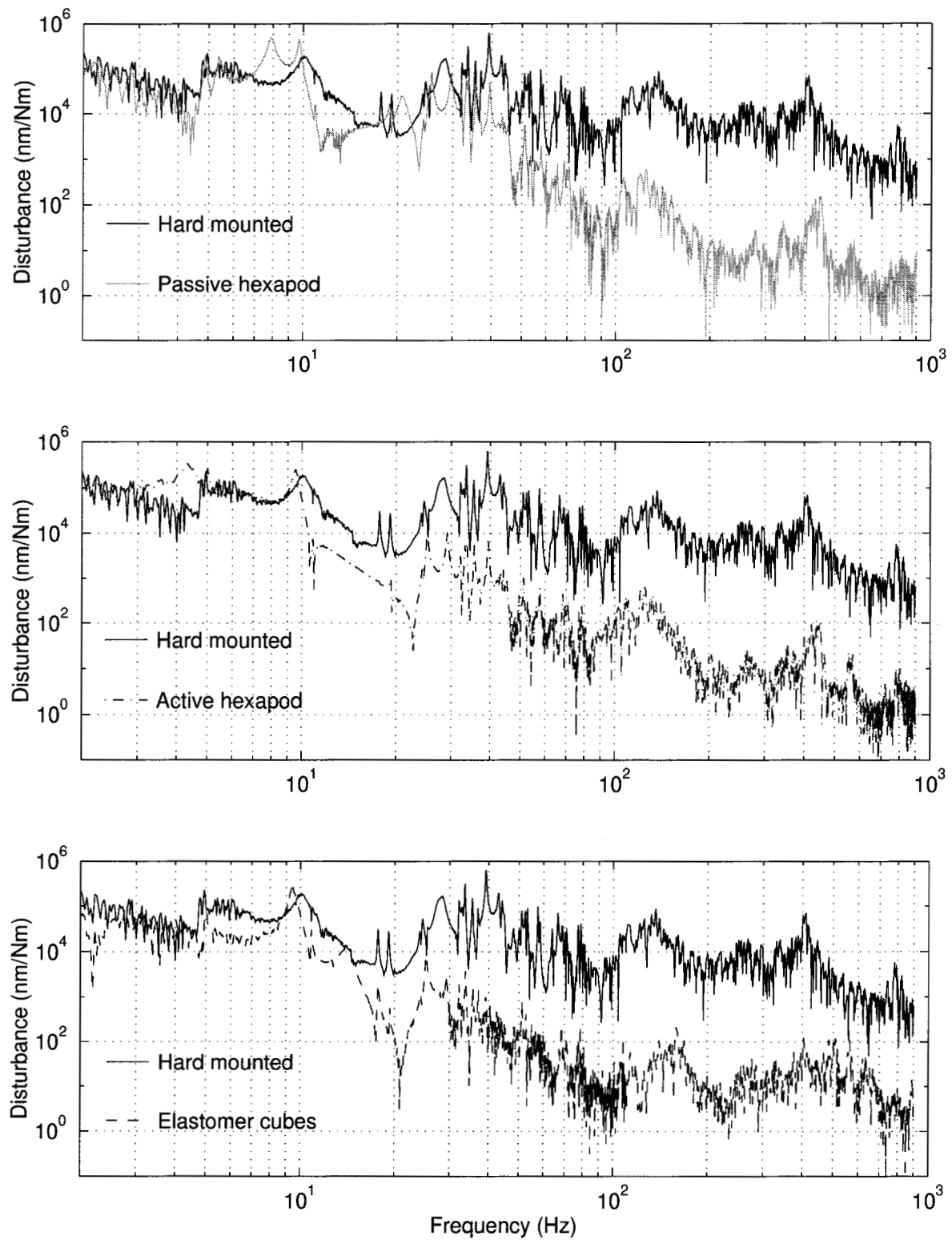
Figure 8. OPD disturbance transfer function - Comparison of the four isolators - input : Y axis torque.
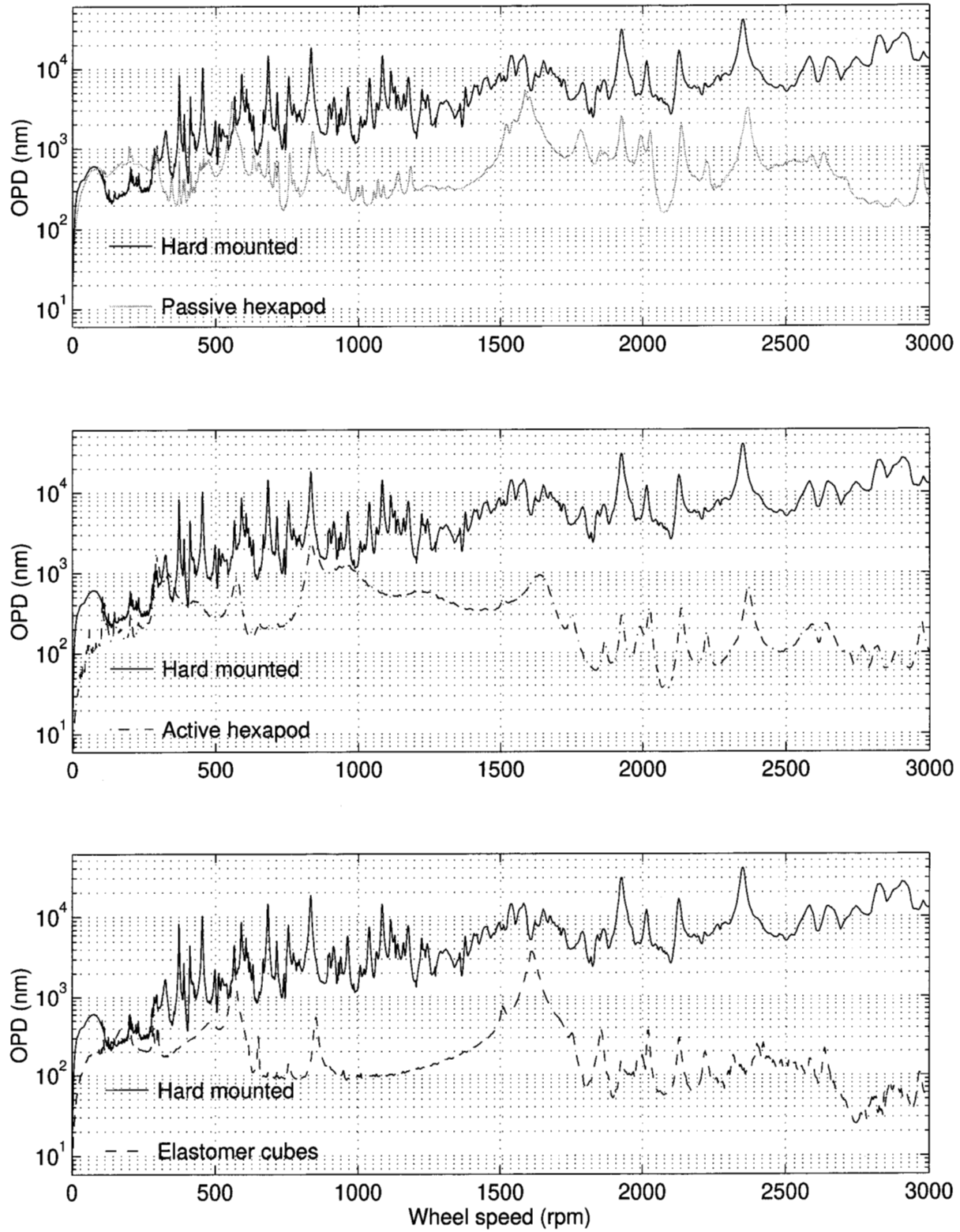
Figure 9. Predicted on-orbit OPD variation as a funtion of the wheel speed - Comparison of the four isolators - All wheel running.